



UNIVERSITY OF LEEDS

This is a repository copy of *Chemical Evolution of CoCrMo Wear Particles: An in Situ Characterization Study*.

White Rose Research Online URL for this paper:
<http://eprints.whiterose.ac.uk/147179/>

Version: Accepted Version

Article:

Koronfel, MA, Goode, AE, Gomez-Gonzalez, MA et al. (8 more authors) (2019) Chemical Evolution of CoCrMo Wear Particles: An in Situ Characterization Study. *Journal of Physical Chemistry C*, 123 (15). pp. 9894-9901. ISSN 1932-7447

<https://doi.org/10.1021/acs.jpcc.9b00745>

© 2019 American Chemical Society. This document is the unedited Author's version of a Submitted Work that was subsequently accepted for publication in *Journal of Physical Chemistry C*, To access the final edited and published work see <https://doi.org/10.1021/acs.jpcc.9b00745>

Reuse

Items deposited in White Rose Research Online are protected by copyright, with all rights reserved unless indicated otherwise. They may be downloaded and/or printed for private study, or other acts as permitted by national copyright laws. The publisher or other rights holders may allow further reproduction and re-use of the full text version. This is indicated by the licence information on the White Rose Research Online record for the item.

Takedown

If you consider content in White Rose Research Online to be in breach of UK law, please notify us by emailing eprints@whiterose.ac.uk including the URL of the record and the reason for the withdrawal request.



eprints@whiterose.ac.uk
<https://eprints.whiterose.ac.uk/>

Chemical Evolution of CoCrMo Wear Particles: an *in-situ* Characterisation

Study

M. A. Koronfel,^a A. E. Goode,^a M. A. Gomez-Gonzalez,^a J. Nelson Weker,^b T. A. Simoes,^c R. Brydson,^c P. Quinn,^d M. F. Toney,^b A. Hart,^e A. E. Porter,^a and M. P. Ryan^{a*}

^{a.} Department of Materials, Imperial College London, London, UK

^{b.} Stanford Synchrotron Radiation Lightsource, SLAC National Accelerator Laboratory, Menlo Park, USA

^{c.} School of Chemical and Process Engineering, University of Leeds, Leeds, UK

^{d.} Diamond Light Source, Didcot, UK

^{e.} Institute of Orthopaedics and Musculoskeletal Science, Royal National Orthopaedic Hospital, London, UK

* m.p.ryan@imperial.ac.uk

Abstract

The unexpected high failure rates of CoCrMo hip-implants is associated with the release of a large number of inflammatory wear particles. CoCrMo is nominally a stable material, however, previous chemical speciation studies on CoCrMo wear particles obtained from periprosthetic tissue revealed only trace amounts of Co remaining despite Co being the major component of the alloy. The unexpected high levels of Co dissolution *in-vivo* raised significant clinical concerns particularly related to the Cr speciation in the dissolution process. At high electrochemical potentials, the alloy's Cr-rich passive film breaks down (transpassive polarisation) facilitating alloy dissolution. The potential release of the carcinogenic Cr(VI) species *in vivo* has been a subject of debate. While the large scale Co dissolution observed on *in vivo* produced particles could indicate a highly oxidising *in vivo* environment, Cr(VI) species were not previously detected in periprosthetic tissue samples (except in the specific case of post-mortem tissue of *diabetic* patients). However, Cr(VI) is likely to be an unstable (transient) species in biological environments and studies on periprosthetic tissue does not provide information on intermediate reaction products nor the exposure history of the wear particles. Here, an *in situ* spectro-microscopy approach was developed, utilising the high chemical resolution of synchrotron radiation, in order to study CoCrMo reactivity as a function of time and oxidising conditions. The results reveal limited Co dissolution from CoCrMo particles, which increases dramatically at a critical electrochemical potential. Furthermore, *in-situ* XAS detected only Cr(III) dissolution, even at potentials where Cr(VI) is known to be produced, suggesting that Cr(VI) species are extremely transient in simulated biological environments where the oxidation zone is small.

1. Introduction

CoCrMo-based hip implants experienced high failure rates despite the high wear and corrosion resistance of the bulk material. Although they exhibited lower volumetric wear compared to the most commonly used metal-on-polyethylene implants, CoCrMo implants produced a larger

number of smaller wear particles as demonstrated in simulation studies.¹ Implant wear particles trigger an immune system inflammatory response which leads to severe pain and the eventual failure of the implants.² The widespread distribution of these particles has been reported as they were observed in hepatic, splenic and cardiac tissue.^{3,4} Additionally, a rise in Co and Cr blood ion levels have also been observed in patients indicating *in vivo* dissolution.^{5,6} CoCrMo particles pose the potential release of cytotoxic and genotoxic Co and Cr ions, thus presenting major clinical risks.⁷

The chemical composition of *in-vivo* produced wear particles was previously examined using multiple spectroscopic techniques on extracted periprosthetic tissue.⁸⁻¹¹ The results consistently found the particles to be predominately composed of Cr(III) species with only trace amounts of Co, despite the original Co: Cr composition ratio being 2:1. The consistent lack of Co in these studies indicates its rapid dissolution, likely as Co(II), which could reach the bloodstream. This high level of Co dissolution was previously unexpected of CoCrMo alloys before they gained regulatory approval. Electrochemically, the bulk alloy exhibits a strong 'Cr-like' passive behaviour due to a surface layer composed mainly of Cr(III) oxide.¹² At high electrochemical potentials the protective surface film breaks due to the transpassive oxidation of Cr(III) to soluble Cr(VI). A recent study revealed the preferential dissolution of Co from alloy particles, accompanied by the development of nanoporous morphology in a process similar to dealloying, but only under transpassive polarisation conditions.¹³ It is known that the immune system's inflammatory response leads to a rise in local electrochemical potential *via* the production of reactive oxygen/nitrogen species^{14,15}, however, it is unclear whether the *in-vivo* inflammatory environment imposes transpassive conditions. The high levels of Co dissolution observed on *in vivo* produced particles could indicate transpassive oxidation which raised major clinical concern due to the transpassive oxidation of Cr(III) to the carcinogenic Cr(VI). This concern has been a subject of debate as Cr(VI) was not previously reported from *in-vivo* samples (only recently, Cr(VI) species were, detected for the first time, on tissue samples of diabetic patients,⁴ who are known to suffer an elevated level of oxidants in their blood¹⁶).

Studies on the composition of the *in vivo* produced particles provide no information on the history of the wear debris, such as length of exposure to the various conditions in the body, and little insight into the intermediate products and mechanisms triggering the inflammatory response. In fact the lack of reported Cr(VI) is not conclusive evidence on its absence *in vivo*, because Cr(VI) is expected to be a transient species which is reduced to Cr(III) once oxidising conditions are removed. The development of an *in situ* approach is therefore essential to study the stages of wear-particle dissolution.

In this work, a combination of synchrotron-based microscopy and spectroscopy techniques were used *in situ* to study the dissolution of CoCrMo in a simulated biological environment, as a function of both time and applied electrochemical potential. The electrochemical potential was applied to mimic the increasingly oxidising local environment caused by the immune inflammatory response. A spectro-microscopy approach was conducted using transmission X-ray microscopy coupled with X-ray absorption spectroscopy (TXM-XAS) at the Stanford Synchrotron Radiation Lightsource (SSRL). Transmission X-ray microscopes are analogous to visible light microscopes but capable of forming images at nanoscale resolution with coupled chemical information: they use diffractive optics such as Fresnel zone plates (a disc

of alternating opaque and transparent concentric rings) to focus the X-rays, and charge-coupled device (CCD) detector to form the images. TXMs produce absorption contrast images displaying the spatial variation of the X-ray transmission through a sample. The probability for absorption of an X-ray, by the target atom, increases sharply when the incident X-ray energy equals the energy required to excite a target electron (photoabsorption). These sharp steps in the absorption coefficient are termed absorption edges. Each element has a characteristic set of absorption edges corresponding to the binding energies of its electrons. The oxidation of an element (higher oxidation states of an element) shifts its absorption edge to a higher X-ray energy. Scanning the X-ray energy across a particular edge in a specific sample gives rise to a distinctive X-ray absorption spectrum (XAS spectra are not only defined by the steps at the binding energies of the elements as other features exist that allow further information about the sample to be extracted but this is outside the scope of this work). Conventional XAS typically uses millimetre-size probes obtaining information from a millimetre-size portion of the sample. Higher spatial resolution measurements are possible with micro and nanoprobe XAS measurements, utilising focused X-ray beams. Here, both locally resolved and volume averaged measurements were utilised to fully explore the reactivity of the wear particles. The high energy resolution of synchrotron radiation is necessary for an accurate speciation analysis, especially with small amounts/nanoscale materials. While electron-based spectro-microscopy (transmission electron microscopy coupled with electron energy loss spectroscopy, TEM-EELS) provides up to atomic-scale spatial resolution, TEM-EELS is limited to a sample thickness of a 100 nm or less and strict vacuum conditions. In addition, water radiolysis by the electron beam produces radicals causing changes in the local chemistry¹⁷ (while Co and Cr X-ray absorption edges are far above that of water). These reasons make the use of liquid cells in TEM challenging. Therefore, in this work, an *in situ* TXM-XAS spectro-microscopy method was developed to study the changes in Co speciation in CoCrMo particles in a simulated biological fluid (SBF) and under an applied electrochemical potential. To complement these data, Cr speciation was examined under similar conditions using conventional XAS.

2. Materials and Methods

2.1. CoCrMo Samples

CoCrMo particles were produced by mechanical ball-milling of the bulk ASTM F75 alloy. Full characterisation of these particles was reported by Simoes *et al.*¹⁸ The particles were stored suspended in isopropyl alcohol at 4 °C. The suspensions were sonicated in a water bath prior to use and subsequently particles were drop-cast on a gold-coated Kapton film (8 µm thick). Drop-casting was performed by pipetting droplets of the suspension on to the gold-Kapton substrate followed by drying the substrate in a low temperature vacuum oven. The gold coating (15 nm thick) was used to act as the working electrode in order to enable application of electrochemical potentials to the CoCrMo particles.

In some studies (for Cr speciation, as explained later) CoCrMo thin films (TFs) were also used. The thin films had a thickness of 80 nm and were utilised as an alternative method to study CoCrMo dissolution at the nanoscale. Thin film thickness is on the scale of particle thickness and provides a form that undergoes both depth and lateral dissolution similar to nanoparticles and unlike *bulk* form. In addition, they provide a larger quantity of material per unit area (compared to disperse particles on a substrate) and hence greater spectroscopy signals. CoCrMo

thin films were grown by sputtering using the LAB 18 thin film deposition system (Kurt J. Lesker), and a CoCrMo sputtering target (Testbourne Ltd, UK) with a composition (63Co 30Cr 7Mo wt%) similar to the biomedical ASTM F75 alloy.

2.2. Simulated Biological Environment

The simulated biological fluid (SBF) was designed to mimic the acidic environment of the lysosomes in macrophage cells; where wear particles are typically found.^{19,20} The SBF had a pH of 5.2 and consisted of 25 mM MES buffer, 0.5 mM CaCl₂·2H₂O, 1 mM MgCl₂, and 200 mM KCl. In some cases, the experiments were repeated with 1 µg/ml of bovine serum albumin added to the SBF (serum-SBF) to study the effect of proteins.

2.3. Co Speciation

Co speciation was studied at the transmission X-ray microscopy beamline 6-2, Stanford Synchrotron Radiation Lightsource (SSRL, USA). The aim of these studies was to monitor spatially resolved Co speciation on CoCrMo particles as a function of potential to determine the onset of Co dissolution.

2.3.1. Electrochemical Cell

A 3D-printed electrochemical cell, previously reported in²¹, was utilised. Briefly, the cell comprised a large reservoir which narrowed down to a 1 mm wide channel which has two, front and back, Kapton-sealed windows facilitating X-ray transmission. The downstream Kapton window was coated with a 15 nm gold layer which acted as the working electrode. CoCrMo particles would have been drop-cast on the gold working electrode as explained earlier in section 2.1. Potentials were applied in 400 s steps from 0.4 to 0.8 V, in 0.1 V increments, (vs Ag/AgCl) to determine the onset of dissolution.

2.3.2. Spectro-microscopy

Transmission X-ray microscopy (TXM) absorbance images of a CoCrMo particle were collected *in situ* and at multiple X-ray energies in order to obtain chemical information (XAS spectra). The transmission X-ray microscope optical design provided a spatial resolution of 30 nm when used with a field of view of ~30 µm; the image acquisition time was ~3 s.

Particle speciation could subsequently be constructed by fitting the measured XAS spectra to the linear combination of the standard XAS spectra of Co and Co(II) edges. Standard Co metal and Co(II) XAS edges were obtained from a Co foil and a CoO powder respectively. Serial image stacks were recorded on a CoCrMo particle: under different conditions: open circuit potential (OCP) and at each applied potential step. The number of photon energies selected for imaging (to obtain one TXM-XAS spectrum) represents the trade-off between accurate chemical analyses versus temporal resolution. In this study, six incident energy points were selected. The first three energies (7659 eV, 7679 eV, and 7699 eV) were pre-edge for the purpose of spectral background removal. The fourth and fifth energies (7710 and 7727 eV) were

used as key spectral differentiation points for the chemical speciation analysis (figure 1(b)). The last energy was 7788 eV, an isosbestic point (where the absorbance intensity is related to the total amount of Co present irrespective of speciation, *i.e.* the particle thickness) at which all data were normalised.

2.4. Cr Speciation

Studies of Cr speciation were designed with the aim of identifying the onset of Cr(VI) release as well as quantifying its transient presence. Cr(VI) absorption is characterised by a sharp pre-edge peak (1 eV wide) which makes it relatively straightforward to distinguish from other Cr valence states (see SI figure S1 of Cr standard spectra). Initially, the studies were conducted in the same TXM-XAS mode used in Co speciation experiments, by measuring changes in absorbance intensity at the Cr(VI) pre-edge peak energy as a function of time and potential (SI figure S2). In these experiments Cr(VI) was not conclusively detected even at electrochemical potentials where it is known to form, and therefore population-averaged (conventional) XAS measurements were carried out to enhance chemical sensitivity. Population-averaged XAS measurements were carried out at Beamline 4-3, SSRL. In addition to CoCrMo particles, CoCrMo 80 nm thin films (TFs) samples were also used. The use of thin films meant that the sample encompassed the full field of view which enhanced the signal to noise ratio, increasing the sensitivity to capture Cr(VI) release.

2.4.1. Electrochemical Cell

The cell was adapted to include a larger front (X-ray entrance) and back (sample) windows which made use of the larger beam size available and increased our sample size. Additionally, the gap between the two windows (X-ray path length) was increased to 3 mm and measurements were carried out in fluorescence geometry. In this setup, when the cell was filled with the simulated biological fluid (SBF), the measurements were only sensitive to signal from the solution (SBF electrolyte) rather than the sample (since the X-ray path length is long enough to cause complete attenuation of the X-ray beam in SBF, SI figure S3). Therefore, this provides measurements of dissolved species only.

2.4.2. Conventional XAS

Conventional (population-averaged) XAS utilised a large beam size of 1 mm x 9 mm. Absorbance intensity at the Cr(VI) pre-edge peak energy was measured as a function of time and potential (time-scan). These were recorded with a 0.33 s temporal resolution. The Cr(VI) pre-edge peak energy was determined to be 5993.25 eV (denoted by E1) using a Cr(VI) standard (10 wt.% Na₂Cr₂O₇ in boron nitride pellet, SI figure S1). Additionally, time scans were also recorded at 6009 eV (above Cr absorption edges, denoted by E2). The scans were recorded under the following electrochemical conditions: first five mins at OCP; followed by 75 mins of applied potential steps (0.4 to 0.8 V in 0.1 V increments); and finally 20 mins at OCP. The OCP of a CoCrMo thin film before applying the electrochemical potential steps is -70 mV while the post-bias OCP is 450 mV.

Furthermore, XANES spectra were recorded in the following instances: dry cells (to present signal of the sample before bias); immediately after adding the electrolyte at OCP (signal of electrolyte before bias); after potential steps were applied (i.e. signal of electrolyte after bias); and finally the samples were detached from the cells and XANES spectra of the samples after bias were recorded.

3. Results

3.1. Co Speciation

A transmission X-ray microscopy (TXM) absorbance image of a CoCrMo particle is shown in figure 1(a). Figure 1(c) shows two representative examples of spectral data obtained from two individual pixels across a selected six-energy image stack. Overall speciation maps could be obtained through fitting measured spectra from each pixel to the linear combination of the standard spectra (shown in figure 1(b)) - $a\text{Co} + b\text{Co(II)}$. The least squares fit weights a, b were calculated per pixel, where b was constrained to $(1-a)$. Therefore, a 2D plot of b presents the spatial distribution maps of Co(II) percentages across the particle, as shown in figure 2(a). The goodness-of-fit was assessed by the R-factor, whereby 95 % of all fitted pixels had a value < 0.05 (see SI figure S4 for a histogram of R-factor values). The overall percentage of Co(II) in the particle could be quantified through the following calculation:

$$\text{Co(II) amount \%} = \frac{\sum_n (b_n \times I_n)}{\sum_n (I_n)} \times 100 \quad (1)$$

Where b is the percentage of Co(II) in an individual pixel n , and I is the absorbance intensity at the isosbestic point. The calculated Co(II) amounts at each potential step are indicated in figure 2(a). The results show a noticeable rise in Co(II) after the 0.8 V step, however, small amounts of Co(II) species were observed at each potential step. Thus, the results suggest a limited Co dissolution at OCP and applied passive potentials followed by a noticeable rise in Co dissolution after 0.8 V transpassive polarisation. The maps show that the highest Co(II) percentages are found at the *edge* regions of the particle. This is possibly due to these regions being less thick (as can be deduced from figure 1(a) by the lower absorbance intensity of the particle's edges compared to particle's core), and hence the oxidised material form higher fractions of the overall material in these regions. In fact, the transmission X-ray microscopy (TXM) image in figure 2(c) shows the egress of diffuse material from the overall surface of the particle and demonstrates the inhomogeneous nature of the dissolution process.

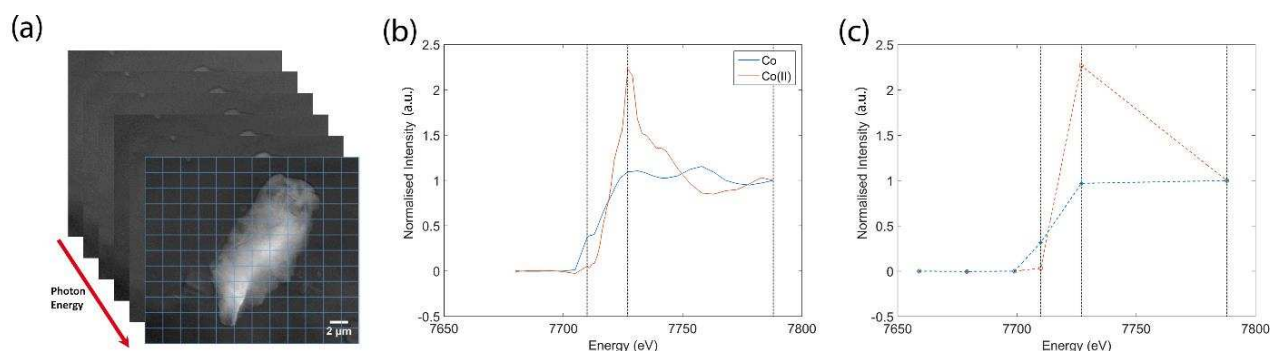


Fig. 1. (a) A stack of TXM absorbance images of a CoCrMo particle recorded at six different energies illustrating the TXM data collection procedure. (b) The recorded standard X-ray absorption spectra for Co metal and Co(II). The black vertical lines illustrate the three post-edge incident X-ray energy points selected for TXM imaging (in addition to three pre-edge energies). (c) Examples of the six-energy spectra of two different sample regions, resembling Co metal absorption (blue) and Co(II) absorption (red).

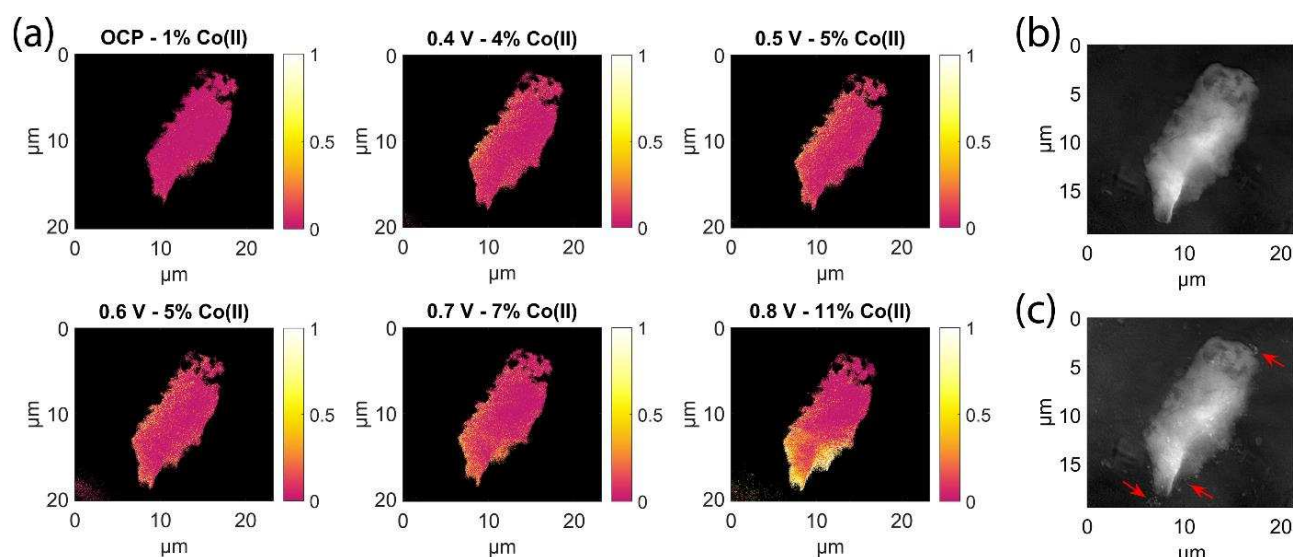


Fig. 2. (a) Speciation maps representing the Co(II) composition fraction of every 30 nm pixel/region in the CoCrMo particle at different applied electrochemical potential. The total Co(II)% (displayed above each corresponding map) were calculated per equation (1) and was found to increase as the applied potential increased, with a noticeable rise at the 0.8 V step. (b-c) TXM images (at the isosbestic X-ray energy) before and during 0.8 V polarisation respectively, showing the egress of diffuse material from the particle.

3.2. Cr Speciation

Figure 3(a) shows the absorbance intensity measured from the simulated biological fluid during polarisation of a CoCrMo thin film sample as a function of time and potential, at both the Cr(VI) pre-edge peak energy (E1) and at 6009 eV (E2). An increase in intensity signal, corresponding to the detection of Cr dissolution into the electrolyte, during the 0.8 V polarisation step (with the onset at 0.7 V) was observed in both cases. However, the increase in signal intensity is approximately 10 times higher at E2 compared to E1. This suggests that the detected

solution species is Cr(III) rather than Cr(VI). The minor intensity rise detected at E1 is likely due to the small pre-edge shoulder of Cr(III) absorption rather than the characteristic pre-edge peak of Cr(VI) (see SI figure S1). Since this dissolution was detected at transpassive potentials, where Cr(VI) is known to be produced, this result reveals the extremely transient nature of Cr(VI) in this environment which would be reduced to Cr(III) either ‘instantly’ or within the negligible time frame of its diffusion away from the sample surface into the detectable electrolyte.

Figures 3(b & c) show the absorbance intensity measured, as a function of time and potential, from SBF and serum-SBF at E2 during the polarisation of CoCrMo thin films (TFs) and particles respectively. The detected increase in absorbance intensity is noticeably higher from TFs (figure 3(b)) compared to particles (figure 3(c)) demonstrating enhanced signal achieved from the use of TFs. In both TFs and particles, the presence of protein resulted in a lower absorbance intensity suggesting that proteins *reduce* Cr dissolution. This is likely due to the formation of an adsorbed protein film on the surface which would restrict metal dissolution.²²

XANES results (figure 4) show a Cr metal signal from CoCrMo thin films in dry cells condition, and no absorption signal after adding the electrolyte at OCP. This shows no detectable dissolution of Cr at OCP (in contrast to Co) and confirms that measurements in wet cell conditions are not sensitive to signal from the sample (which would have contributed a Cr signal). The XANES obtained after polarisation reveal a Cr(III) signal from the electrolyte, and a ‘mixed’ XANES spectra from thin films indicating the presence of solid oxidised Cr species on the thin film surfaces (consistent with sensitivity to the passive oxide). The XANES of post-bias thin films (TFs) were fitted using a linear combination of the corresponding TFs dry cell (represents the original state of the thin film) and electrolyte post-bias (represents the oxidised species resulting from the polarisation of the thin film). The fit results and weights are illustrated in figure 5 and table 1, showing a greater percentage of oxidised species on the TF which reacted in SBF compared to the one which reacted in serum-SBF, again suggesting that the presence of protein restricted the Cr reactivity.

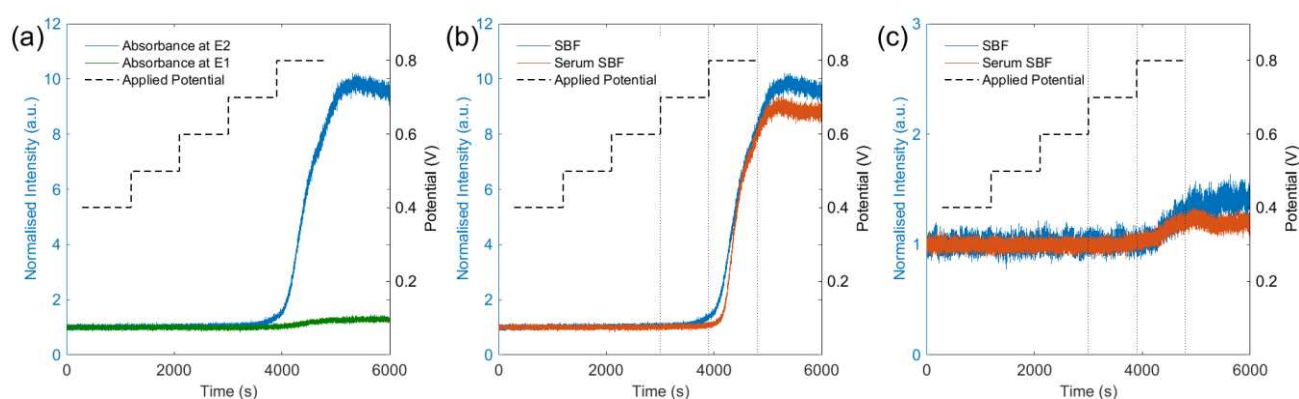


Fig. 3. (a) Absorbance intensity as a function of time and potential recorded at both the Cr(VI) pre-edge peak energy 5993.25 eV (E1) and at 6009 eV (E2), during the polarisation of CoCrMo TF. A greater increase in the absorbance intensity signal at E2 suggests that the detected dissolution is likely Cr(III) species rather than Cr(VI). (b-c) Absorbance intensity as a function of time and potential recorded at E2 from in

both SBF and serum-SBF during polarisation of CoCrMo TF (b) and particles (c). A comparison between the detected dissolution in SBF and serum-SBF, in both TF and particles, shows less detected dissolution in the presence of serum. The system was at OCP at the end of the 0.8 V step.

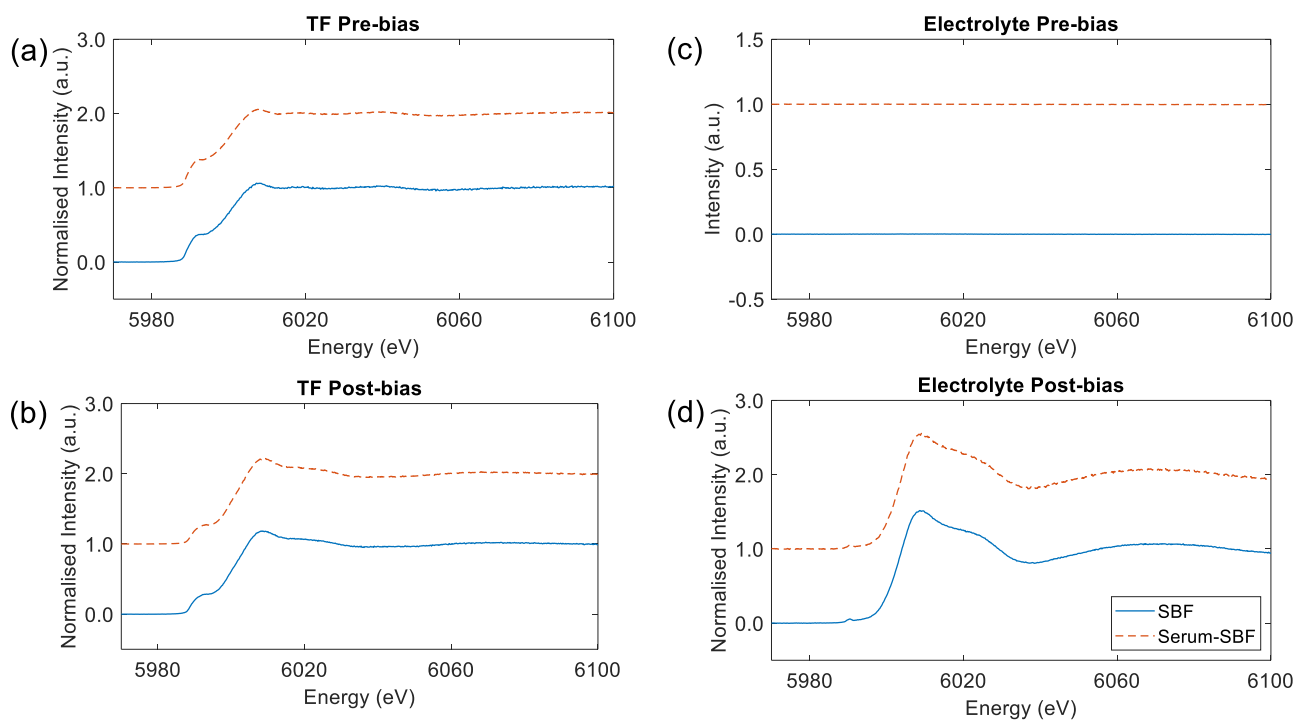


Fig. 4. XANES spectra of TF and electrolyte before and after potential application in both the SBF (blue) and serum-SBF (red). The SBF and serum-SBF spectra are offset for clarity.

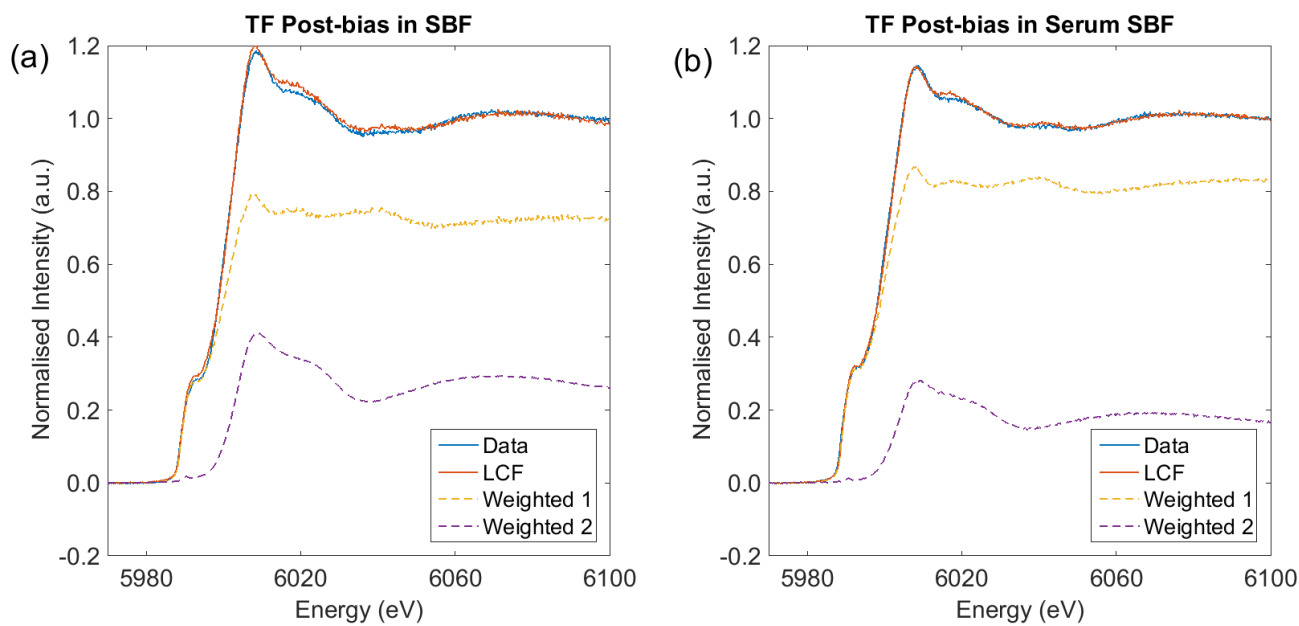


Fig. 5. XANES spectra of TF biased in SBF (a) and serum-SBF (b) overlaid with fit results obtained by a linear combination of the TF pre-bias (original TF state, Weighted 1) and electrolyte post-bias (oxidised species, Weighted 2) spectra. The data shows a greater ratio of oxidised Cr on the surface of the TF biased in SBF compared to serum-SBF.

Table 1: LCF parameters for both TF biased in SBF and serum-SBF

	TF pre-bias	Electrolyte post-bias	R-factor
TF biased in SBF	0.725	0.275	0.000825
TF biased in serum-SBF	0.821	0.179	0.000369

4. Discussion

4.1. Technical Aspects

The combination of TXM-XAS is a powerful spectro-microscopy approach for studying the reactivity of nanoscale systems. In this work, spatially resolved chemical information was obtained on a single CoCrMo particle at the Co edge. Although highly resolved X-ray absorption spectra were collected of the Co standards, only six selected energies were used for imaging the CoCrMo particle. Selecting only a few key energy points that distinguish between the species of interest greatly improved the temporal resolution of the measurements which in turn allowed studying changing chemistry *in situ*.

TXM-XAS measurements at the Cr edge are more challenging compared to Co: the lower X-ray energy of the Cr edge means a lower transmitted intensity signal, combined with the low analyte concentration in a spatially resolved measurements of a single particle which resulted in an undetectable absorption signal at the Cr edge. In fact, even conventional XAS of a population of particles yielded a relatively low signal to noise ratio (figure 3(c)) when compared to the measurement conducted on an 80 nm thin film (figure 3(b)). The conclusions obtained from the measurements conducted on both thin film and particles were similar and hence, thin films are potentially a viable alternative when studying materials' degradation at the nanoscale.

4.2. Potential *In-vivo* Implications

The limited Co dissolution observed, here, during passive polarisation suggests that a large-scale *in vivo* Co dissolution (as reported from wear particles extracted after implant failure¹¹) is likely due to the local inflammatory environment imposing transpassive polarisation conditions. This hypothesis is also supported by the morphological development of particles polarised above 0.6 V (vs Ag/AgCl) which was found to be analogous to the morphology of *in vivo* produced particles.¹³ The onset of Cr dissolution observed here is consistent with the

increase in Co dissolution kinetics, confirming that the increase in Co dissolution is facilitated by the perturbation of the alloy's Cr-rich passive film.

Real time *in situ* measurements of Cr dissolution suggested that the detected dissolved species was Cr(III) despite the onset of dissolution occurring under transpassive polarisation (where Cr(VI) is known to be produced). It is known that Cr(VI) is reduced in biological environments to Cr(III).²³ The aim of this work was to quantify this transient nature of Cr(VI) species, and the results suggest the reduction of Cr(VI) is instantaneous. Here, this transient nature is likely related to the rapid diffusion of Cr(VI) species away from the electrode surface (the oxidising environment) into the electrolyte, however under *in vivo* conditions the reduction would be related to diffusion away from the local inflammation. Therefore, the carcinogenic Cr(VI) species may potentially persist *in vivo* for longer periods depending on the nature and extent of the inflammatory environment. Recently, Cr(VI) species were detected (for the first time) in post-mortem tissue from hip implant patients who had been diabetic.⁴ It was hypothesised that the elevated levels of reactive oxygen species in the blood of diabetic patients have led to the re-oxidation of Cr(III) back to Cr(VI).

The presence of protein inhibited Cr dissolution from both thin films and particles. The protective effect of protein is hypothesised to be due to the formation of metal-protein-hydroxide complex adsorbed on the surface and restricting metal dissolution.²² However, it is noted that this is in contrast to Mo behaviour where the presence of protein led to increased dissolution.²⁴ Furthermore, it is possible that the observed protective impact of protein is only a short-term effect (few hours). Recent studies found that the effect of protein on the corrosion of Ti6Al4V was time dependent, where enhanced metal release was observed only after 24 hours.^{25,26} This is related to the kinetics of metal-protein interactions. For instance, the formation of protein-metal bonds on the surface oxide layer of stainless steel was relatively sluggish and the subsequent detachment of metal-protein complexes from the surface was an even slower process.^{27,28} Thus, enhanced metal release in the presence of protein may be observed in longer-term studies. Hedberg²⁹ suggested that increasing both time and oxidative conditions may cause a negative shift on the effect of protein on metal alloy degradation (from suppressing to enhancing dissolution). Direct interaction of proteins with the metal surface (as opposed to the oxide layer) is more rapid and hence protein may lead to faster dissolution in non-passive conditions. Here, the positive effect of protein on Cr dissolution was observed even in transpassive conditions, albeit after a relatively short period of time.

5. Conclusions

In conclusion, the results showed a continuous dissolution of Co from CoCrMo particle, which dramatically increased in the transpassive regime. The results suggest that the *in vivo* dissolution of CoCrMo wear debris may be an autocatalytic process, where extensive dissolution is only observed in strongly oxidising conditions, likely triggered by the inflammatory response to the particle. Although the initial dissolution of Co is small, given the large number of wear particles, this dissolution could activate the immune system response. The subsequent production of peroxy-like radicals leads to an increasingly oxidising environment and accelerated dissolution. The large-scale Co dissolution

observed, after implants' failure, in periprosthetic wear particles¹¹ is likely facilitated by the breakdown of the Cr-rich passive film, suggesting that transpassive dissolution occurs *in vivo*. Here, *in situ* Cr dissolution was captured in the transpassive regime using XAS. High temporal resolution scans at two different energies suggested that the detected species was Cr(III) indicating that Cr(VI) is extremely transient in these simulated conditions. *In vivo* produced Cr(VI) species are likely to be reduced to Cr(III) once it has diffused away from the inflammatory regions of high reactive oxygen species concentration.

Supporting Information

The supporting information document contains four supplementary figures: firstly, the measured standard X-ray absorption spectra of Cr(III) and Cr(VI) species; secondly, the absorption intensity as a function of time and potential recorded at Cr(VI) pre-edge energy at the SSRL TXM beamline 6-2; thirdly, a schematic of the signal measurement set up at SSRL XAS beamline 4-3; and finally, histograms of R-factor values for Co speciation spectral fitting.

Acknowledgements

MAK was supported by the EPSRC Centre for Doctoral Training in Advanced Characterisation of Materials (grant number EP/L015277/1). MPR acknowledges funding from the Royal Academy of Engineering and Shell Global Solutions *via* the Research Chair Scheme.

Use of the Stanford Synchrotron Radiation Lightsource, SLAC National Accelerator Laboratory, is supported by the U.S. Department of Energy, Office of Science, Office of Basic Energy Sciences under Contract No. DE-AC02-76SF00515.

References

- (1) Catelas, I.; Boby, J. D.; Medley, J. B.; Krygier, J. J.; Zukor, D. J.; Huk, O. L. Size, Shape, and Composition of Wear Particles from Metal-Metal Hip Simulator Testing: Effects of Alloy and Number of Loading Cycles. *J. Biomed. Mater. Res. A* **2003**, *67* (1), 312–327.
- (2) Konttinen, Y. T.; Pajarinen, J. Surgery: Adverse Reactions to Metal-on-Metal Implants. *Nat. Rev. Rheumatol.* **2013**, *9* (1), 5–6.
- (3) Urban, R. M.; Tomlinson, M. J.; Hall, D. J.; Jacobs, J. J. Accumulation in Liver and Spleen of Metal Particles Generated at Nonbearing Surfaces in Hip Arthroplasty. *J. Arthroplasty* **2004**, *19* (8), 94–101.
- (4) Swiatkowska, I.; Mosselmans, J. F. W.; Geraki, T.; Wyles, C. C.; Maleszewski, J. J.; Henckel, J.; Sampson, B.; Potter, D. B.; Osman, I.; Trousdale, R. T.; et al. Synchrotron Analysis of Human Organ Tissue Exposed to Implant Material. *J. Trace Elem. Med. Biol.* **2018**, *46*, 128–137.
- (5) De Smet, K.; De Haan, R.; Calistri, A.; Campbell, P. A.; Ebramzadeh, E.; Pattyn, C.; Gill, H. S. Metal Ion Measurement as a Diagnostic Tool to Identify Problems with Metal-on-Metal Hip Resurfacing. *J. Bone Jt. Surg.* **2008**, *90* (Supplement 4), 202–208.
- (6) Hart, A. J.; Sabah, S. A.; Bandi, A. S.; Maggiore, P.; Tarassoli, P.; Sampson, B.; Skinner, J. A. Sensitivity and Specificity of Blood Cobalt and Chromium Metal Ions for Predicting Failure of Metal-on-Metal Hip Replacement. *J. Bone Jt. Surgery, Br. Vol.* **2011**, *93* (10), 1308–1313.
- (7) Gill, H. S.; Grammatopoulos, G.; Adshead, S.; Tsiologianis, E.; Tsiroidis, E. Molecular and Immune Toxicity of CoCr Nanoparticles in MoM Hip Arthroplasty. *Trends Mol. Med.* **2012**, *18* (3), 145–155.
- (8) Huber, M.; Reinisch, G.; Trettenhahn, G.; Zweymüller, K.; Lintner, F. Presence of Corrosion Products and Hypersensitivity-Associated Reactions in Periprosthetic Tissue after Aseptic Loosening of Total Hip Replacements with Metal Bearing Surfaces. *Acta Biomater.* **2009**, *5* (1), 172–180.
- (9) Catelas, I.; Campbell, P. A.; Boby, J. D.; Medley, J. B.; Huk, O. L. Wear Particles from Metal-on-Metal Total Hip Replacements: Effects of Implant Design and Implantation Time. *Proc. Inst. Mech. Eng. Part H J. Eng. Med.* **2006**, *220* (2), 195–208.
- (10) Hart, A. J.; Sandison, A.; Quinn, P.; Sampson, B.; Atkinson, K. D.; Skinner, J. A.; Goode, A.; Powell, J. J.; Mosselmans, J. F. W.

- Microfocus Study of Metal Distribution and Speciation in Tissue Extracted from Revised Metal on Metal Hip Implants. *J. Phys. Conf. Ser.* **2009**, *190*, 012208.
- (11) Goode, A. E.; Perkins, J. M.; Sandison, A.; Karunakaran, C.; Cheng, H.; Wall, D.; Skinner, J. A.; Hart, A. J.; Porter, A. E.; McComb, D. W.; et al. Chemical Speciation of Nanoparticles Surrounding Metal-on-Metal Hips. *Chem. Commun.* **2012**, *48* (67), 8335.
 - (12) Hodgson, A. W. E.; Kurz, S.; Virtanen, S.; Fervel, V.; Olsson, C. O. A.; Mischler, S. Passive and Transpassive Behaviour of CoCrMo in Simulated Biological Solutions. *Electrochim. Acta* **2004**, *49* (13), 2167–2178.
 - (13) Koronfel, M. A.; Goode, A. E.; Weker, J. N.; Tay, S. E. R.; Stitt, C. A.; Simoes, T. A.; Mosselmans, J. F. W.; Quinn, P.; Brydson, R.; Hart, A.; et al. Understanding the Reactivity of CoCrMo-Implant Wear Particles. *npj Mater. Degrad.* **2018**, *2* (1), 8.
 - (14) Hosman, A. H.; van der Mei, H. C.; Bulstra, S. K.; Busscher, H. J.; Neut, D. Effects of Metal-on-Metal Wear on the Host Immune System and Infection in Hip Arthroplasty. *Acta Orthop.* **2010**, *81* (5), 526–534.
 - (15) Behl, B.; Papageorgiou, I.; Brown, C.; Hall, R.; Tipper, J. L.; Fisher, J.; Ingham, E. Biological Effects of Cobalt-Chromium Nanoparticles and Ions on Dural Fibroblasts and Dural Epithelial Cells. *Biomaterials* **2013**, *34* (14), 3547–3558.
 - (16) Niedowicz, D. M.; Daleke, D. L. The Role of Oxidative Stress in Diabetic Complications. *Cell Biochem. Biophys.* **2005**, *43* (2), 289–330.
 - (17) Schneider, N. M.; Norton, M. M.; Mendel, B. J.; Grogan, J. M.; Ross, F. M.; Bau, H. H. Electron–Water Interactions and Implications for Liquid Cell Electron Microscopy. *J. Phys. Chem. C* **2014**, *118* (38), 22373–22382.
 - (18) Simoes, T. A.; Goode, A. E.; Porter, A. E.; Ryan, M. P.; Milne, S. J.; Brown, A. P.; Brydson, R. M. D. Microstructural Characterization of Low and High Carbon CoCrMo Alloy Nanoparticles Produced by Mechanical Milling. *J. Phys. Conf. Ser.* **2014**, *522* (1), 012059.
 - (19) Doorn, P. F.; Campbell, P. A.; Worrall, J.; Benya, P. D.; McKellop, H. A.; Amstutz, H. C. Metal Wear Particle Characterization from Metal-on-Metal Total Hip Replacements: Transmission Electron Microscopy Study of Periprosthetic Tissues and Isolated Particles. *J. Biomed. Mater. Res.* **1998**, *42* (1), 103–111.
 - (20) Delaunay, C.; Petit, I.; Learmonth, I. D.; Oger, P.; Vendittoli, P. A. Metal-on-Metal Bearings Total Hip Arthroplasty: The Cobalt and Chromium Ions Release Concern. *Orthop. Traumatol. Surg. Res.* **2010**, *96* (8), 894–904.
 - (21) Tay, S. E. R.; Goode, A. E.; Nelson Weker, J.; Cruickshank, A. A.; Heutz, S.; Porter, A. E.; Ryan, M. P.; Toney, M. F. Direct in Situ Observation of ZnO Nucleation and Growth via Transmission X-Ray Microscopy. *Nanoscale* **2016**, *8*, 1849–1853.
 - (22) Khan, M. A.; Williams, R. L.; Williams, D. F. The Corrosion Behaviour of Ti-6Al-4V, Ti-6Al-7Nb and Ti-13Nb-13Zr in Protein Solutions. *Biomaterials* **1999**, *20* (7), 631–637.
 - (23) Shah, K. M.; Quinn, P. D.; Gartland, A.; Wilkinson, J. M. Understanding the Tissue Effects of Tribo-Corrosion: Uptake, Distribution, and Speciation of Cobalt and Chromium in Human Bone Cells. *J. Orthop. Res.* **2015**, *33* (1), 114–121.
 - (24) Simoes, T. A.; Bryant, M. G.; Brown, A. P.; Milne, S. J.; Ryan, M.; Neville, A.; Brydson, R. Evidence for the Dissolution of Molybdenum during Tribocorrosion of CoCrMo Hip Implants in the Presence of Serum Protein. *Acta Biomater.* **2016**, *45*, 410–418.
 - (25) Zhang, Y.; Addison, O.; Yu, F.; Troconis, B. C. R.; Scully, J. R.; Davenport, A. J. Time-Dependent Enhanced Corrosion of Ti6Al4V in the Presence of H₂O₂ and Albumin. *Sci. Rep.* **2018**, *8* (1), 3185.
 - (26) Hedberg, Y. S.; Žnidaršič, M.; Herting, G.; Milošev, I.; Odnevall Wallinder, I. Mechanistic Insight on the Combined Effect of Albumin and Hydrogen Peroxide on Surface Oxide Composition and Extent of Metal Release from Ti6Al4V. *J. Biomed. Mater. Res. Part B Appl. Biomater.* **2018**, *107B*, 858–867.
 - (27) Hedberg, Y.; Karlsson, M. E.; Blomberg, E.; Odnevall Wallinder, I.; Hedberg, J. Correlation between Surface Physicochemical Properties and the Release of Iron from Stainless Steel AISI 304 in Biological Media. *Colloids Surfaces B Biointerfaces* **2014**, *122*, 216–222.
 - (28) Hedberg, Y.; Karlsson, M.-E.; Wei, Z.; Žnidaršič, M.; Odnevall Wallinder, I.; Hedberg, J. Interaction of Albumin and Fibrinogen with Stainless Steel: Influence of Sequential Exposure and Protein Aggregation on Metal Release and Corrosion Resistance. *Corrosion* **2017**, *73* (12), 1423–1436.
 - (29) Hedberg, Y. S. Role of Proteins in the Degradation of Relatively Inert Alloys in the Human Body. *npj Mater. Degrad.* **2018**, *2* (1), 26.

TOC Graphic

